Chemical Engineering Journal 532 (2026) 174378

Contents lists available at ScienceDirect

Chemical Engineering Journal

journal homepage: www.elsevier.com/locate/cej

AI-driven fault diagnosis in smart bearings using mosaic-patterned electret for multi-modal motion sensing

Longwei Duan [a,b,1], Xinhui Mao [a,b,1], Yuxiang Dong [a,b,1], Haiyang Yu [a,b], Jiyuan Zhang [a,b], Shuyu Zhang [a,b], Yiqun Gu [a,b], Yingwen Li [a,b], Kaifeng Ding [a,b], Zhiheng Wang [a,b], Xingxu Zhang [a,b], Honglong Chang [a,b], Lihua Tang [c], Jin Wu [d,***], Wenbin Huang [e,**], Kai Tao [a,b,*]

[a] *Ministry of Education Key Laboratory of Micro and Nano Systems for Aerospace, School of Mechanical Engineering, Northwestern Polytechnical University, Xi'an, 710072, PR China*
[b] *Shenzhen Research Institute of Northwestern Polytechnical University, Sanhang Science & Technology Building, No.45th, Gaoxin South 9th Road, Nanshan District, Shenzhen City, 518057, PR China*
[c] *Department of Mechanical and Mechatronics Engineering, The University of Auckland, 5 Grafton Road, Auckland, 1010, New Zealand*
[d] *State Key Laboratory of Optoelectronic Materials and Technologies and the Guangdong Province Key Laboratory of Display Material and Technology, School of Electronics and Information Technology, Sun Yat-sen University, Guangzhou, 510275, PR China*
[e] *State Key Laboratory of Mechanical Transmission for Advanced Equipment, Chongqing University, Chongqing, 400030, PR China*

ARTICLE INFO

Keywords:
Smart bearing sensor
Self-powered sensor
Mosaic-patterned electret
Multi-modal monitoring
Signal decoupling

ABSTRACT

Smart bearings offer a promising approach for real-time motion and condition monitoring in rotating machinery by embedding sensing functionality directly into the bearing structure. However, most existing smart bearing designs remain constrained to single-modal motion sensing, typically capturing only rotational or vibrational motion. In this paper, a novel smart thrust ball bearing (STBB) is proposed, incorporating a mosaic-patterned polarized electret for enhanced multi-modal motion sensing. Charges are injected into the electret film in a patterned manner using silicon shadow masks fabricated via deep reactive ion etching (DRIE). The coupled signal from simultaneous rotational and vibrational motions is fully decoupled through the dual Fourier transform (DFT) algorithm. The results show that the STBB exhibits high linearity, with $R^2 = 0.9999$ and $R^2 = 0.9998$ for rotation and vibration, respectively, and a rotational sensitivity of 7.48 rpm·Hz^{-1}. The STBB is further integrated into a six-joint robotic arm for dynamic monitoring. Combined with a long short-term memory (LSTM) neural network, the STBB achieves 90.33% fault classification accuracy. These findings highlight its potential as a scalable and multi-modal sensing solution for intelligent maintenance systems.

1. Introduction

Bearings are critical components in mechanical systems, playing an essential role in ensuring operational stability and reliability across industries such as aerospace [1,2], robotics [3,4], and energy manufacturing [5]. However, prolonged operation often leads to various failure modes in bearings, including wear [6–8], corrosion [9–11], cracking [12–14], and misalignment [15]. Therefore, bearing condition monitoring is crucial for preventing unexpected failures and maintaining long-term system performance [16]. Traditional monitoring methods typically rely on externally mounted, battery-powered sensors to track operating status. Nonetheless, these systems often face challenges such as structural complexity, signal degradation, and high maintenance demands [17–19]. To address these challenges, self-

* Corresponding author at: Ministry of Education Key Laboratory of Micro and Nano Systems for Aerospace, School of Mechanical Engineering, Northwestern Polytechnical University, Xi'an, 710072, PR China.
** Correspondence to: W. Huang, State Key Laboratory of Mechanical Transmission for Advanced Equipment, Chongqing University, Chongqing, 400030 China.
*** Correspondence to: J. Wu, State Key Laboratory of Optoelectronic Materials and Technologies and the Guangdong Province Key Laboratory of Display Material and Technology, School of Electronics and Information Technology, Sun Yat-sen University, Guangzhou 510275, PR China.
E-mail addresses: l.tang@auckland.ac.nz (L. Tang), wujin8@mail.sysu.edu.cn (J. Wu), whuang@cqu.edu.cn (W. Huang), taokai@nwpu.edu.cn (K. Tao).
[1] These authors contributed equally to this work.

https://doi.org/10.1016/j.cej.2026.174378
Received 13 December 2025; Received in revised form 2 February 2026; Accepted 18 February 2026
Available online 20 February 2026
1385-8947/© 2026 Elsevier B.V. All rights are reserved, including those for text and data mining, AI training, and similar technologies.

powered smart bearings have gained attention as a promising solution to reduce mechanical complexity and enhance resistance to signal degradation [20].

Recently, smart bearing sensors with various self-powered sensing mechanisms have been explored, including triboelectric [21–28], electromagnetic [29–33], piezoelectric [34–36], and electrostatic [37–40] approaches. Among these mechanisms, triboelectric self-powered sensing offers a simple structural design, broad material compatibility, and high responsiveness to high-frequency contact excitation, making it well suited to rotational and friction-induced monitoring scenarios [41–44]. Han et al. [45] proposed a bearing-integrated triboelectric nanogenerator based on rolling contact, where periodic contact and separation between steel balls and a polytetrafluoroethylene (PTFE)-coated surface induce charge generation. The device achieved a peak power output of 20 μW and demonstrated a high sensitivity of 0.998 $Hz{\cdot}rpm^{-1}$ by directly mapping signal frequency to bearing speed. Qin et al. developed a hybrid smart cage system combining piezoelectric patches and a triboelectric sleeve. The piezoelectric elements fabricated from lead zirconate titanate (PZT) generated 16.92 μW, while the triboelectric sleeve delivered a higher output of 83.08 μW. This system enabled bearing fault classification through six-fold frequency harmonics, achieving an accuracy of up to 99.8%. Choi et al. [46] designed a roller-based triboelectric bearing, where sliding friction between PTFE rollers and interdigitated electrodes generated alternating current (AC). At 400 rpm, an open-circuit voltage of 45 V was observed, with each 15° rotation corresponding to one pulse for angular displacement tracking. Electromagnetic self-powered sensing provides stable signal generation and excellent durability under high-speed rotation, enabling reliable long-term monitoring in harsh mechanical environments. Zhang et al. [47] developed a 17-tooth variable reluctance energy harvester, converting 4.17 Hz mechanical rotation into a 71 Hz electrical signal via periodic permeability modulation. Combined with a 50 g-range accelerometer, the system detected vibration deviations ranging from 0.76 to 2.83 g. Wang et al. [48] introduced an eccentric rotor electromagnetic device utilizing a friction pendulum structure, achieving a power density of 1982 $W{\cdot}m^{-3}$, with synchronized three-phase voltages enabling the detection of imbalance faults. Piezoelectric self-powered sensing delivers strong electromechanical coupling and high sensitivity to dynamic strain, allowing accurate detection of vibration-induced changes in bearing systems. Zhang et al. [49] integrated arc-shaped piezoelectric elements directly into the bearing outer ring, utilizing the d33 mode to generate 131 μW under 20 Hz vibration. Fault diagnosis was performed via spectral analysis of the outer ring passing frequency, which was three times the rotation frequency. Guan et al. [50] designed a rotary impact-type piezoelectric device, where a limiting frame constrained vibration amplitude within a 1.5 mm gap, producing 825 μW at a rotational speed of 13.5 Hz. Electrostatic self-powered sensing features minimal mechanical wear, compact device structure, and stable charge retention, making it ideal for embedded and maintenance-free monitoring. Li et al. [51] developed a $BaTiO_3$/polyimide (BTO/PI) nanocomposite thin-film sensor capable of inferring lubrication status through dielectric constant variations. The system achieved a rotational speed measurement error below 0.26%, and its printed circuit board (PCB)-integrated design enabled dual-modal sensing of speed and temperature. Collectively, these studies have significantly advanced the development of self-powered smart bearing sensors. Triboelectric-based designs, while widely adopted due to their simple integration, flexible material selection, and strong responsiveness to frictional excitation, still face challenges such as wear-induced performance degradation, signal instability under fluctuating contact conditions, and susceptibility to environmental factors such as humidity. Piezoelectric approaches offer high energy conversion efficiency and excellent sensitivity to dynamic strain, yet their relatively low power output and the brittleness of ceramic materials pose limitations for seamless integration into compact bearing assemblies. Electromagnetic mechanisms, though capable of delivering comparatively higher power and long-term durability, typically require bulky magnetic components, making miniaturization and structural embedding difficult. Moreover, two critical challenges continue to hinder further progress in this field. On the one hand, existing systems predominantly employ single-mode sensing, focused on either vibration or rotational speed, thus failing to capture the intricately coupled dynamic behaviors present under actual operating conditions. On the other hand, the lack of structural adaptability in current sensor designs makes it difficult to tailor monitoring systems to various bearing types or constrained installation environments.

To address the abovementioned limitations, a novel smart thrust ball bearing (STBB) sensor system is proposed in this paper. The STBB integrates an electrostatic sensing module with a modular mosaic-patterned electret sensing structure, enabling non-contact energy transduction while simultaneously capturing both rotational and vibrational responses. This compact architecture can also be applied to double-row deep groove ball bearings (dr-DGBB) by adjusting the electret film polarization scheme, facilitating deployment across diverse mechanical environments. A dual Fourier transform (DFT) algorithm is developed to decouple the coupled signal, effectively separating rotational and vibrational features in the time-frequency domain. To further enhance condition recognition under varying load and motion states, a long short-term memory (LSTM) neural network is used for fault classification and is trained on an experimentally collected dataset of multimodal bearing responses. The STBB is integrated into a six-joint robotic arm testbed and experimentally validated under simulated industrial conditions, featuring variable-speed actuation, fluctuating payloads, and other fault-inducing scenarios. Experimental results validate the system's effectiveness in real-time condition monitoring, demonstrating robust mechanical adaptability and high diagnostic accuracy. This work provides technical support for the advancement of next-generation self-powered smart bearing sensor technologies and offers a scalable and versatile option for predictive maintenance systems.

2. Results and discussion

2.1. *Structure design and working principle of the STBB*

Mosaic structures are known for their high degree of patterning, discreteness, and reconfigurability. These features have led to their widespread adoption in fields such as image processing and decorative design. Their fundamental units can be flexibly assembled into complex configurations, offering excellent structural freedom and geometric adaptability [52]. Inspired by this concept, the unitized characteristics of mosaic patterns are introduced into the design of flexible electret films made of fluorinated ethylene propylene (FEP). As shown in Fig. 1a, disc-shaped and cylindrical electret structures are derived, respectively, by conceptually transforming mosaic patterns through in-plane and out-of-plane twisting. The disc-shaped electret film is fabricated by planar patterned polarization using a radial-sector mask, resulting in a tiled charge layout within the 2D plane. In contrast, the cylindrical electret film is obtained by first patterning a planar film using a 2D grid-like mask, and then curling it out of the plane into a tubular geometry, thereby forming an azimuthally distributed charge array on the curved surface. These modes form disc-shaped and cylindrical electret film structures, which are integrated into thrust and double-row deep groove ball bearings, respectively, for motion state monitoring in industrial robotic production lines. The thrust ball bearing, which is often required to bear axial loads, is typically installed at the base of robotic arms. The working principle of this bearing under rotational and radial vibration modes is illustrated in Fig. S1a. Correspondingly, dr-DGBB is generally installed at the hook end of the robotic arm to ensure the stable operation of the hook. The working principle of this bearing under rotational and axial vibration modes is shown in Fig. S1b.

Moreover, the disc-shaped and cylindrical electret films undergo patterned polarization processes to achieve an orderly and arrayed charge distribution. Specifically, the disc-shaped electret film is first

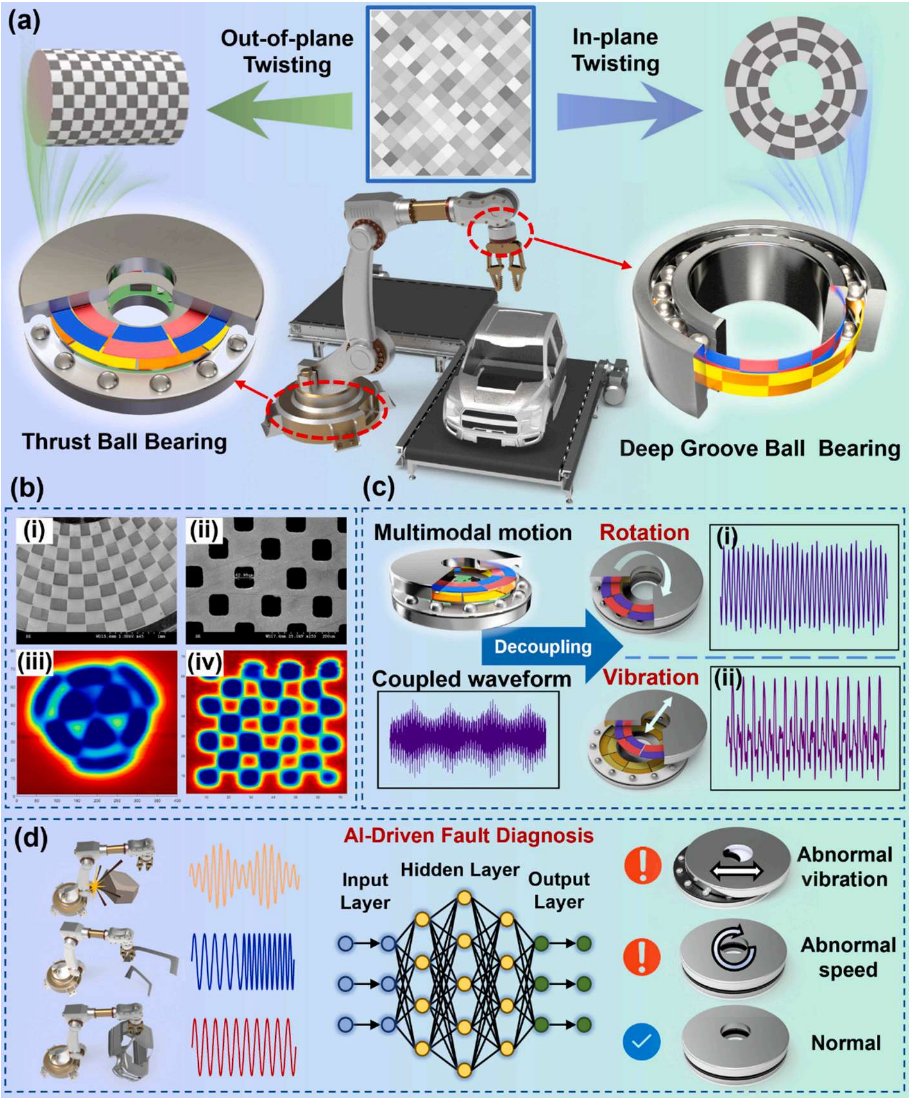

Fig. 1. Structural design and intelligent monitoring of smart thrust ball and deep groove bearings. (a) Applications of thrust ball bearings and deep groove ball bearings in industrial automotive production lines. (b) Polarization and characterization of mosaic-patterned electret films: i) Polarization mask for the disc-shaped electret film; ii) Polarization mask for the cylindrical electret film; iii) Surface potential distribution of the polarized disc-shaped electret film; iv) Surface potential distribution of the polarized cylindrical electret film. (c) Multimodal signal decoupling of the STBB: i) Separated signal under rotational mode; ii) Separated signal under vibrational mode. (d) AI-driven fault diagnosis system based on STBB.

polarized using a dedicated mask (Fig. 1b-i), enabling the formation of a radially segmented charge distribution. Likewise, for the cylindrical electret film, a custom mask (Fig. 1b-ii) is employed during corona charging to produce an array of charges aligned along the circumferential direction. This patterned distribution forms after the film is curled into a cylindrical shape. The resulting surface potential profiles for the two structures are shown in Fig. 1b-iii and b-iv, respectively. It can be observed that the electret surfaces have been pattern-polarized. The polarized regions exhibit lower surface potential due to the presence of more negative charges. These patterned and polarized electret film structures are of great significance for enabling subsequent multimodal monitoring of bearing dynamics. The proposed dedicated electrode structure exhibits a spatial distribution similar to that of the mosaic-patterned electret. Moreover, the electrode units are interconnected in an interleaving manner to form two integrated electrode groups, which serve as the positive and negative terminals that are connected to the signal acquisition circuit. Combined with a spatial distribution strategy tailored for bearing dynamics and an application-specific mounting scheme, the design provides robust sensing capabilities under both single-mode and compound motion conditions. Considering the similar coupling mechanisms of rotation and vibration observed in both bearing types, along with the relatively simple structure of the STBB, an experimental analysis of its electrical output under compound motion conditions is conducted. As shown in Fig. 1c, when circumferential rotation and radial vibration occur simultaneously, the resulting electrical signals overlap at the electrode interface, leading to distinct waveform coupling. To facilitate accurate separation of rotational and vibrational components, the DFT algorithm is developed to extract the respective rotation (Fig. 1c-i) and vibration (Fig. 1c-ii) signal components, enabling multi-parameter joint monitoring under complex dynamic conditions.

Bearings often suffer from various faults under complex working conditions, which can affect the normal operation of industrial equipment and even lead to major safety accidents. Therefore, intelligent monitoring and fault diagnosis of bearing conditions are of vital importance. Consequently, the fault diagnosis system based on the LSTM neural network is designed, as shown in Fig. 1d. When industrial equipment such as robotic arms encounters external shocks, falling workpieces, or other unexpected events, the STBB generates corresponding output signals. By collecting experimental data under various scenarios, the LSTM network is trained to recognize these signals. The STBB ultimately demonstrates accurate identification of five fault types, including abnormal vibration and abnormal rotational speed. This greatly improves the efficiency and convenience of maintenance during real-world equipment operation.

The electromechanical behavior of the STBB under circumferential rotation is analytically derived to provide a detailed theoretical foundation for the operating principle. The schematic diagram of this rotational mode is shown in Fig. S1c. The surface potential of the charged electret film can be expressed as:

$$V_0 = \frac{Q_0}{C_0} \tag{1}$$

where Q_0 is the amount of charge stored in the electret film, and C_0 is the capacitance of the electret film. The amount of charge stored in the electret film can also be expressed as:

$$Q_0 = \sigma_0 S \tag{2}$$

where σ_0 is the surface charge density of the electret film, and S is the charging area. The capacitance of the electret film can be expressed as:

$$C_0 = \frac{\varepsilon_r \varepsilon_0 S}{d_0} \tag{3}$$

where d_0 is the thickness of the electret film, ε_0 is the vacuum permittivity, and ε_r is the relative permittivity of the electret film. Substituting Eqs. (2) and (3) into Eq. (1), the following expression is obtained:

$$\sigma_0 = \frac{\varepsilon_r \varepsilon_0 V_0}{d_0} \tag{4}$$

Thus, the surface charge density of the electret can be determined by measuring the surface potential. According to the principle of electrostatic induction, the charge stored in the electret film induces net charges on the electrodes and the electret substrate. Since the electret is closer to the electret substrate, more charges are attracted to the substrate than to the electrodes. However, the charges that are actually transferred through the external circuit are determined by variations in the induced charges on the electrodes, while most of the induced charges on the electret substrate remain immobilized. Consequently, the effective charge density on the electrode is significantly lower than the surface charge density on the electret film. At the initial position shown in Fig. S1, the electrodes are aligned with both the positively and negatively charged regions of the electret film. Therefore, when the electret film assembly rotates by an angle θ, the induced charge on the electrode can be expressed as:

$$Q_E(\theta) = \begin{cases} \frac{1}{2} n\mu\sigma_0 (r_1^2 - r_0^2)\theta + (-\mu\sigma_0)\left[S_0 - \frac{1}{2} n (r_1^2 - r_0^2)\theta\right] & \theta \in \left[0, \frac{\pi}{n}\right) \\ \mu\sigma_0 \left[2S_0 - \frac{1}{2} n (r_1^2 - r_0^2)\theta\right] + (-\mu\sigma_0)\left[\frac{1}{2} n (r_1^2 - r_0^2)\theta - S_0\right] & \theta \in \left[\frac{\pi}{n}, \frac{2\pi}{n}\right) \end{cases} \tag{5}$$

where S_0 is the sector area of a single electrode, n is the number of electrode sectors, θ is the rotational angle from the initial time $t = 0$, μ is a corrected induction factor introduced to reflect the effective charge density induced on the electrodes, and r_0 and r_1 are the inner and outer radii of the electrodes, respectively. Based on the induced charge relationship shown in Eq. (5), the dependency of induced charge on rotational angle can be further derived by incorporating expressions for the sector area and angular velocity.

Given that the air gap between the electret film and the electrode is significantly smaller than the electrode area, the system can be approximated as a variable capacitance structure. Consequently, the bipolar electret-based rotary generator can be equivalently modeled as an AC voltage source in series with a capacitor. By establishing the voltage-charge relationship and applying Kirchhoff's voltage law, the dynamic behavior of charge transfer and current output over a rotation cycle can be theoretically obtained. Building upon these results, a Taylor expansion under two limiting conditions allows us to derive closed-form expressions for the short-circuit current and open-circuit voltage, respectively:

$$I_{SC} = \begin{cases} \mu\sigma_0 (r_1^2 - r_0^2) n\omega, & t \in \left[0, \frac{\pi}{n\omega}\right) \\ \mu\sigma_0 (r_1^2 - r_0^2) nw, & t \in \left[\frac{\pi}{n\omega}, \frac{2\pi}{n\omega}\right) \end{cases} \tag{6}$$

$$U_{OC} = \begin{cases} \frac{\mu\sigma_0 (r_1^2 - r_0^2)}{2C}(2n\omega t - \pi), & t \in \left[0, \frac{\pi}{n\omega}\right) \\ -\frac{\mu\sigma_0 (r_1^2 - r_0^2)}{2C}(2n\omega t - 3\pi), & t \in \left[\frac{\pi}{n\omega}, \frac{2\pi}{n\omega}\right) \end{cases} \tag{7}$$

These analytical expressions describe the characteristic output behavior of the bipolar electret-based rotary generator under ideal load conditions and serve as a theoretical foundation for subsequent experimental validation and performance analysis.

2.2. Fabrication and assembly process

An exploded view of the STBB is presented in Fig. 2(a). The seat ring serves as the mounting platform for the patterned electret film. Above the seat ring, bearing balls and a cage facilitate smooth rotational motion, while the shaft ring at the top is connected to a substrate. A sampling circuit is mounted above the substrate, with the copper electrodes affixed below. The structural and motion relationship of key components is further illustrated in Fig. S2. The key structural parameters of the STBB are listed in Table S1. The assembled STBB is shown in Fig. 2b, with arrows indicating the positions of the copper electrodes and electret film. The structural parameters and physical appearance of the patterned electrodes used in the STBB are presented in Fig. S3. The step-by-step assembly process of the STBB is presented in Fig. S4, highlighting the integration of rolling elements, electrodes, and housing components. A selective corona discharge system, consisting of a shadow mask and multiple discharge needles, is developed to introduce a charge distribution into the electret film (Fig. 2c). This patterning charging technique eliminates the need for microfabrication or etching of the electret film itself. A tungsten needle array serves as both the discharge electrodes and the grid for uniform charge injection. Deep reactive ion etching (DRIE) is employed to create microscale openings on a silicon substrate, forming the shadow mask. A 300 nm gold layer is deposited as the conductive top grid, and a 500 nm SiO_2 layer serves as the insulating bottom layer. During the charging process, the shadow mask is positioned on top of the electret film, with a gold-electrode-coated silicon substrate underneath, enabling selective charge injection. The distance between the needles and the mask is maintained at 5–10 mm, and the substrate electrode is grounded.

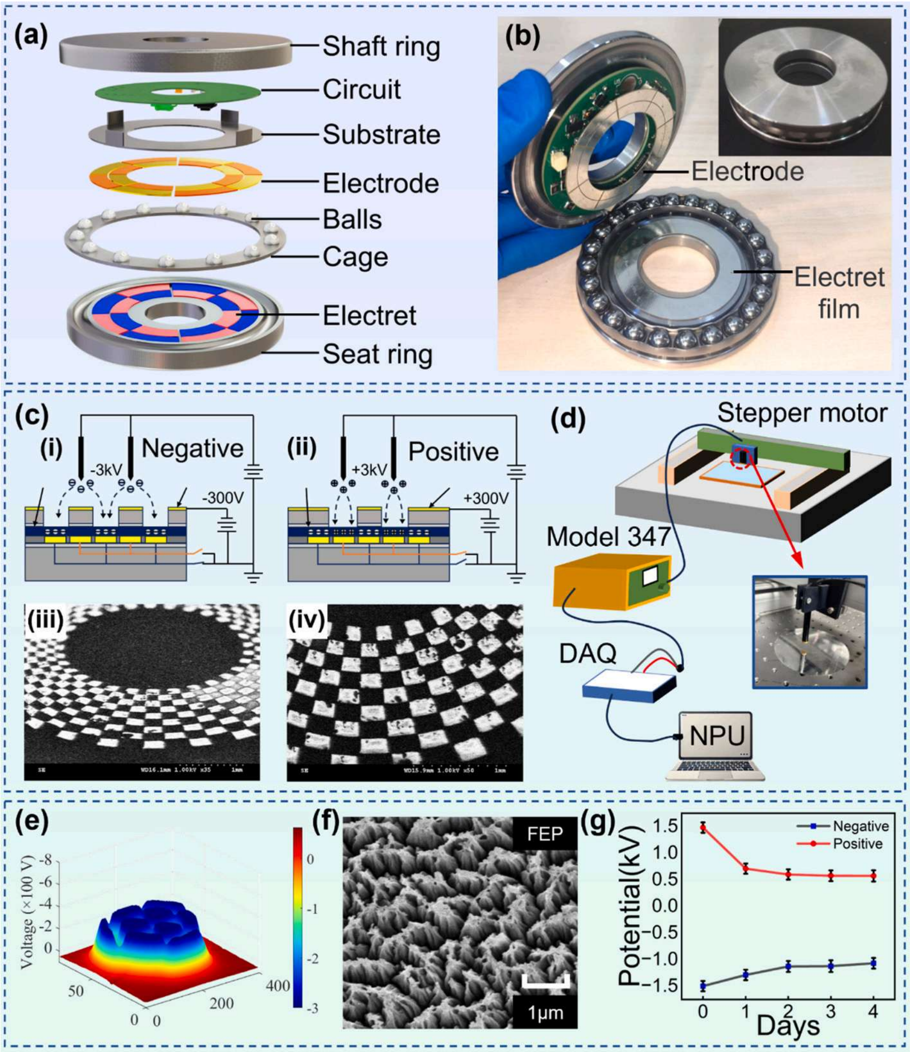

Fig. 2. Fabrication and assembly of the STBB. (a) Exploded view of the STBB, showing the shaft ring, sampling circuit, electret, electrode, and related components. (b) Photograph of the assembled STBB, highlighting the electrode and electret film. (c) Charging process of the electret film: i) negative discharge, ii) positive discharge, iii) SEM image of negatively charged regions, and iv) magnified SEM image of the negatively charged regions. (d) Schematic diagram of the 3D surface potential scanning system utilizing the Trek Model 347 probe. (e) 3D potential distribution map of the negatively charged electret film. (f) SEM image of the FEP surface microstructure. (g) Stability of the surface potential on bipolar-charged electret films during 96 h of static storage at room temperature.

In the bipolar discharge process, the FEP is first negatively charged and then positively charged. During negative discharge, voltages of approximately −3 kV and −300 V are applied to the needle and the mask, respectively (Fig. 2c-i). Negative ions generated at the needle tips migrate through the mask openings and become embedded in the exposed regions of the electret film. Afterward, the mask is repositioned to cover the pre-charged areas and expose new regions for positive discharge, during which the applied voltages are switched to +3 kV and +300 V (Fig. 2c-ii). The SEM image reveals a high-resolution micro-patterned charge distribution (Fig. 2c-iii). As shown in the magnified SEM image (Fig. 2c-iv), the bright regions correspond to areas polarized by negative charges. The charged and uncharged regions form a well-defined ring-shaped array with clearly distinguishable boundaries. These results confirm that the charge patterns can be precisely controlled by modifying the mask design. Charged and uncharged areas are indicated by bright and dark regions, respectively, reflecting excellent pattern uniformity.

To characterize the effectiveness of the selective corona discharge process, a non-contact electrostatic voltmeter is utilized to construct a surface potential scanning system, as depicted in Fig. 2d. The probe is positioned 1–3 mm above the electret film and mounted on an automated platform for scanning and data acquisition. The measured surface potential distribution after negative charging is shown in Fig. 2e, indicating that the negative charges are successfully implanted and excellent surface potentials are obtained. Fig. 2f presents the SEM image of the electret film surface, highlighting its nanostructured morphology. The stability of the surface potential on bipolar-charged electret films is monitored over a 96-hour period of static storage at room temperature, as shown in Fig. 2g. The initial surface potential decreases from approximately 1500 V to 800 V within the first 24 h, after which the decay rate slowed significantly. After 96 h, the surface potentials stabilize at approximately −1020 V for negative regions and +650 V for positive regions. This asymmetry is attributed to the higher charge retention capability of the FEP material for negative charges compared to positive charges.

2.3. Multimodal output performance evaluation

Recognizing the importance of validating multimodal sensing under realistic conditions, a comprehensive test platform is developed to simulate various dynamic scenarios and capture the electrical output of the STBB. As shown in Fig. 3a, the test platform integrates the STBB, a

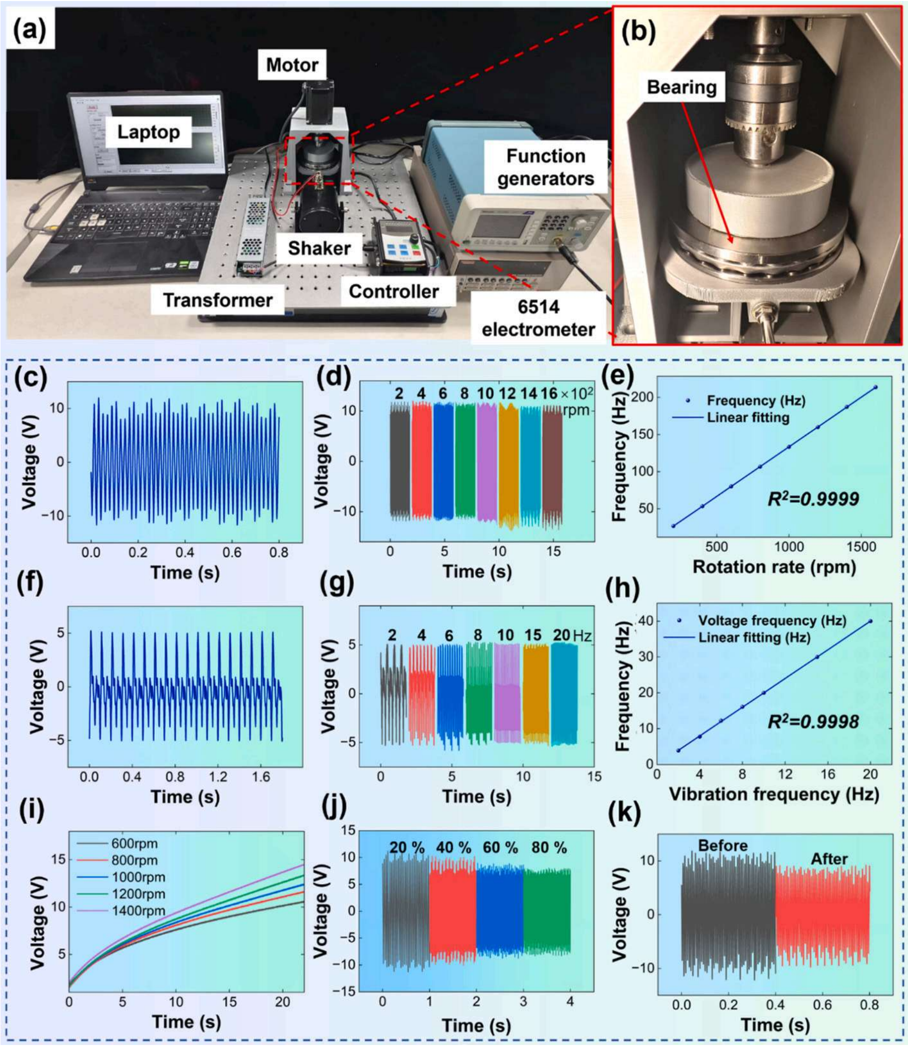

Fig. 3. Electrical output performance testing of the STBB (a) The STBB test platform, including the motor, transformer, bearing, function generator, vibration exciter, and Keithley 6514 electrometer. (b) Enlarged view of the bearing installation. (c) Output signal of the STBB at 400 rpm. (d) Output signals of the STBB across a speed range of 200 to 1600 rpm. (e) Fitted curve of output signal frequency versus rotational speed. (f) Output signal of the STBB under 10 Hz radial vibration. (g) Output signals of the STBB under radial vibrations ranging from 2 to 20 Hz. (h) Fitted curve of signal frequency versus vibration frequency. (i) Charging curve of a 2.2 μF capacitor. (j) Output signal variation under different humidity levels. (k) Output signal comparison before and after 200,000 rotation cycles.

rotational motor, and a vibration exciter, along with essential instruments for signal control and electrical output acquisition. The motor provides adjustable rotational inputs, while the vibration exciter introduces variable-frequency and amplitude disturbances, emulating real-world multimodal operating conditions. This platform supports performance evaluation, signal decoupling validation, and algorithm testing. The installation setup of the STBB within the test platform is shown in Fig. 3b. The base of the bearing is rigidly fixed to the platform via a substrate, which is mechanically coupled to the vibration exciter for adjustable radial excitation. The upper shaft ring is connected to the motor output shaft to enable continuously adjustable rotation. Fig. 3c presents the output voltage waveform at a motor speed of 400 rpm. Under rotational excitation, the STBB generates a stable and symmetrical alternating signal with peak voltages of approximately 10 V, demonstrating its structural stability and the consistent AC output capability of the embedded electret-based generator under single-mode rotation. Fig. 3d illustrates the output waveforms across a speed range of 200 to 1600 rpm under pure rotational motion without external radial vibration. Peak voltages remain consistently around 10 V with slight fluctuation, demonstrating the system's robustness across a wide rotational range and its suitability for diverse monitoring scenarios.

As indicated by the earlier observations, the output signal frequency of the STBB appears to be closely related to rotational speed. To explore this relationship in more detail, a fast Fourier transform (FFT) is applied to the output signals, and a frequency-speed curve is fitted, as shown in Fig. 3e. The results reveal a highly linear trend with a correlation coefficient of $R^2 = 0.9999$. The fitted equation is $y = 0.13366{\cdot}x - 0.21814$, indicating a frequency sensitivity of 7.48 $rpm{\cdot}Hz^{-1}$, validating the system's effectiveness and precision in rotational speed measurement. For radial vibration sensing, an external vibration exciter was employed to generate controlled radial vibrations without rotational input. Fig. 3f illustrates the output signal under a vibration frequency of 10 Hz with a constant amplitude. Under this radial excitation, the system generates a periodic AC signal. In contrast to the symmetrical waveform obtained under pure rotation, this vibration-induced waveform exhibits a distinct asymmetry. The resulting signal frequency corresponds precisely to the applied excitation frequency. Fig. 3g displays the output signals under radial vibrations ranging from 2 to 20 Hz, where the consistent peak locations and amplitudes further confirm the robustness of the sensor for single-modal vibration monitoring. The FFT is applied to analyze the relationship between vibration frequency and output signal, and the resulting frequency-response curve is subsequently fitted, as shown in

Fig. 3h. The results demonstrate a highly linear frequency response with a fitted equation of $y = 2.00351 \cdot x - 0.04302$ and a correlation coefficient of $R^2 = 0.9998$, confirming the system's capability for precise radial vibration monitoring. Table S2 summarizes the comparison between actual and measured values of rotational speed and vibration frequency.

In addition to sensing capabilities, the STBB's energy harvesting performance and environmental lifetime characteristics are also explored. To evaluate long-term energy harvesting performance, the STBB is used to charge a 2.2 μF capacitor. As shown in Fig. 3i, at a rotation speed of 1400 rpm, the capacitor voltage increased to 14.44 V within 22 s, demonstrating efficient conversion of mechanical energy into electrical storage. The impact of environmental humidity on system performance is also investigated. As shown in Fig. 3j, with increasing humidity, the output amplitude decreased slightly from 11.16 V to 8.03 V, due to minor charge leakage from the electret surface. Finally, a durability test involving 200,000 continuous rotations is conducted. As illustrated in Fig. 3k, the peak voltage exhibited a slight decline from 11.57 V to 8.97 V, while the signal frequency remained unchanged, demonstrating the STBB's long-term reliability.

2.4. Multimodal coupled signal decoupling

Bearings often operate under compound motion conditions involving both rotation and vibration in practical applications. To accurately monitor bearing conditions under compound motion conditions, it is essential to decouple the coupled signal resulting from simultaneous rotational and vibrational inputs. As illustrated in Fig. 4a, the DFT algorithm implemented in the STBB is capable of achieving such signal decoupling. The results show that when the STBB undergoes compound motion involving both rotation and vibration, the resulting signal manifests as a high-frequency carrier modulated by a low-frequency envelope. The rotational state of the STBB can be directly extracted using the FFT, which identifies the dominant frequency components of the high-frequency carrier. In contrast, vibrational information is obtained indirectly, that is, the envelope of the coupled signal is first extracted to isolate the low-frequency modulation component, and a second FFT is then performed on the envelope to retrieve vibration-related features.

Compound motion experiments are conducted on the STBB to evaluate the effectiveness of the proposed DFT algorithm. During testing, the

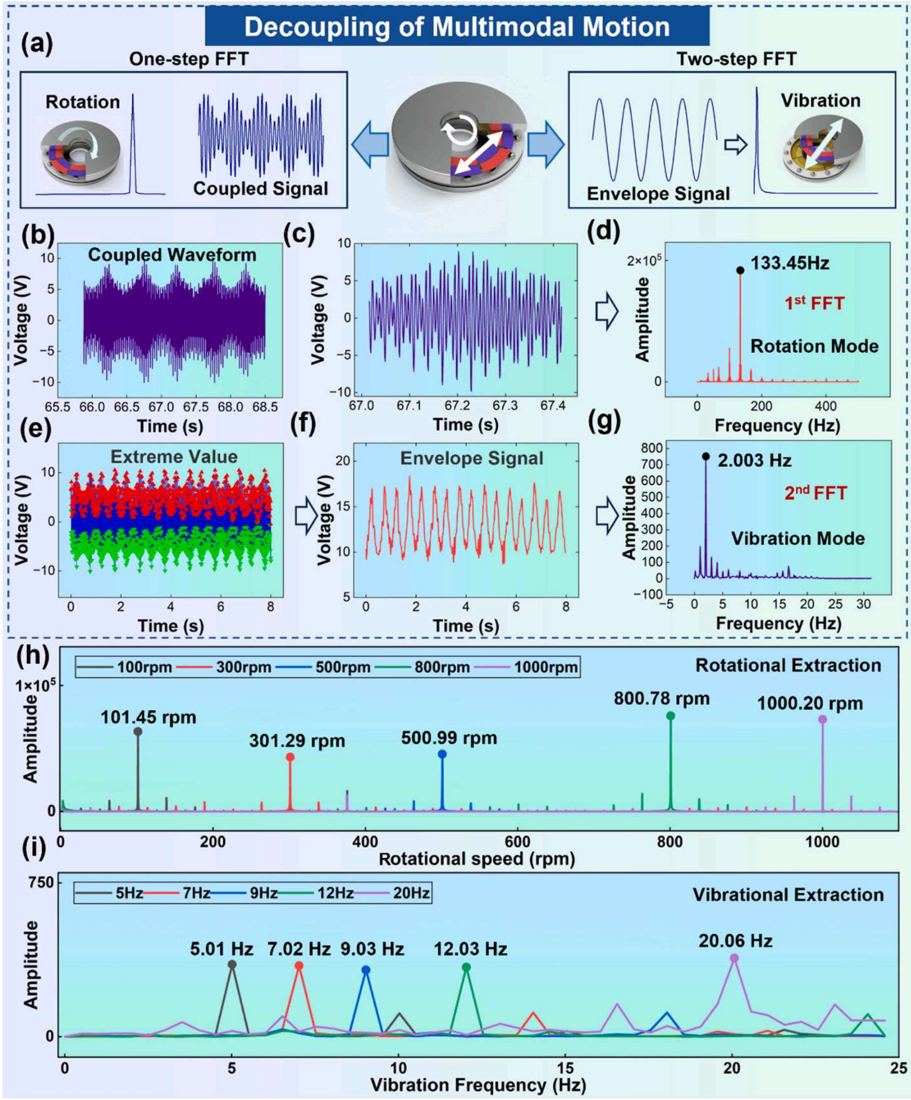

Fig. 4. Multimodal motion signal decoupling process for the STBB. (a) Signal decoupling flow based on the DFT algorithm. (b) Coupled signals generated under simultaneous rotation and vibration. (c) Single-period waveform of the composite signal. (d) Frequency spectrum from the first Fourier transform. (e) Peak-to-peak extraction from the coupled signal. (f) Extracted waveform of peak-to-peak amplitude variation. (g) Frequency spectrum from the second Fourier transform. (h) Extraction of different rotational speeds under the same vibration condition in the STBB. (i) Extraction of different vibration conditions under the same rotational speed in the STBB.

STBB is subjected to simultaneous rotation at 1000 rpm and radial vibration at 2 Hz. This combined motion generates a coupled signal, as shown in Fig. 4b, which exhibits a high-frequency oscillation modulated by a low-frequency waveform with clear periodicity. Fig. 4c presents a single-cycle segment of the coupled signal, clearly displaying high-frequency oscillations with alternating voltage polarity and well-defined peaks and troughs. The low-frequency vibration component induces periodic amplitude modulation on the high-frequency carrier. The DFT algorithm is then applied to decouple the signal components. First, the FFT is performed on the raw signal to extract the primary frequency content. As shown in Fig. 4d, a prominent spectral peak is observed at 133.45 Hz. According to the fitted equation in Fig. 3e, this frequency corresponds to a calculated rotational speed of 997.74 rpm. Compared with the reference setting of 1000 rpm, the relative error is only 0.23%, confirming the high accuracy of the rotational signal extraction.

The peaks and troughs of the original coupled signal are first identified to extract vibration-related information, as shown in Fig. 4e. The peak-to-peak waveform is then calculated, which reflects the modulation effect induced by radial vibration, as illustrated in Fig. 4f. A second FFT is performed on the resulting amplitude signal. The frequency spectrum, shown in Fig. 4g, reveals a dominant frequency component at

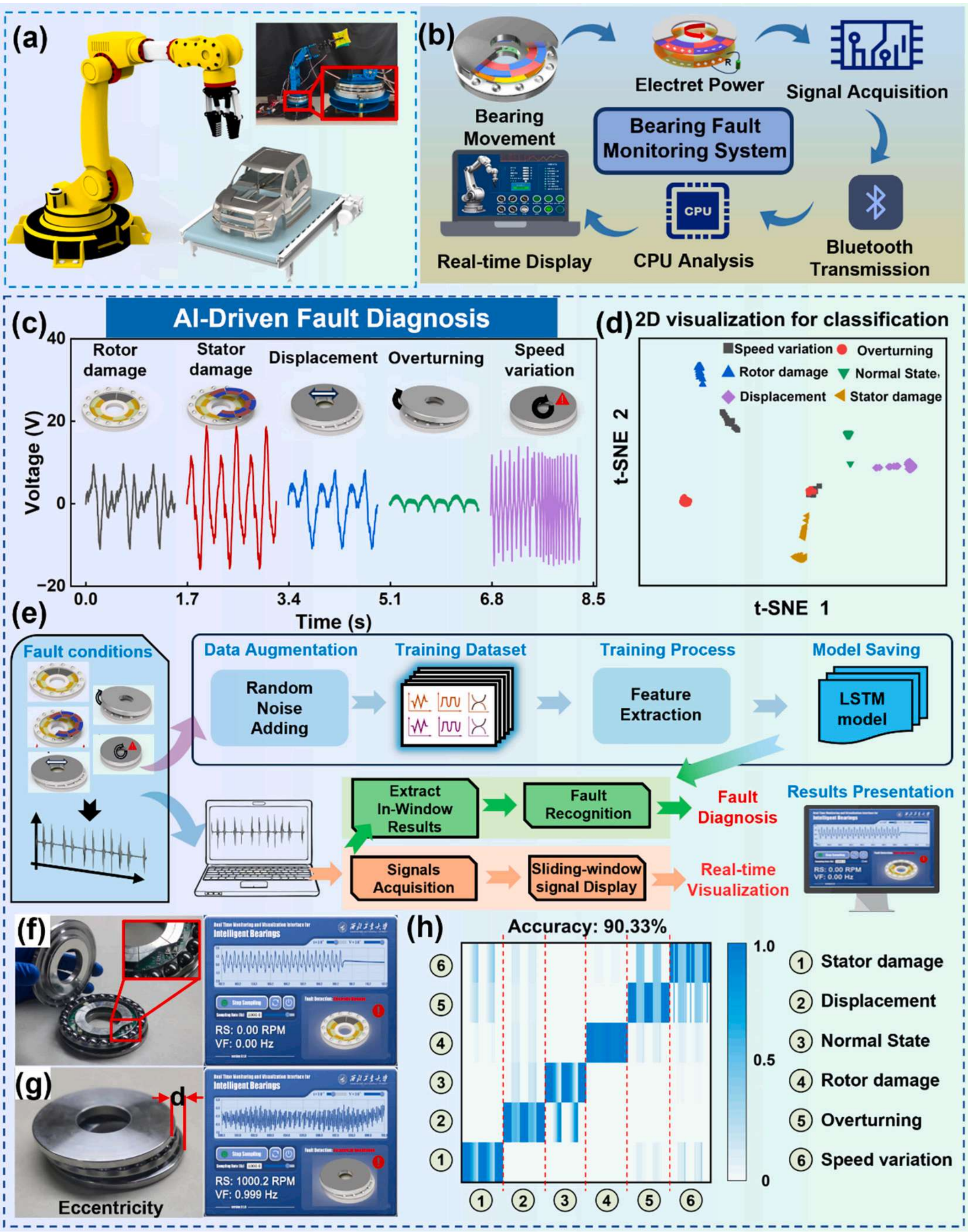

Fig. 5. Industrial application and fault monitoring experiments of the STBB (a) Application of the STBB in the robotic arm of an automotive assembly line. (b) Workflow of the STBB fault monitoring system in an industrial scenario. (c) STBB output waveforms under five typical bearing fault conditions. (d) t-SNE visualization of feature embeddings from the fully connected layer for different fault categories. (e) AI-driven fault diagnosis workflow based on STBB signal processing and LSTM learning. (f) Voltage signal and real-time display interface warning under the STBB electrode damage condition. (g) Voltage signal and real-time display interface warning under the STBB installation eccentricity. (h) Confusion matrix of LSTM-based fault diagnosis for aix operating scenarios.

2.003 Hz. When compared to the externally applied excitation of 2 Hz, the relative error is just 0.15%. These results validate the reliability of the proposed method in accurately extracting low-frequency vibration features from the coupled signal. In conclusion, the DFT algorithm effectively separates rotational and vibrational components in the coupled signal. This confirms the capability of the algorithm to perform accurate multimodal signal decoupling under complex motion conditions.

Recognizing the need to evaluate performance under more complex dynamics, two supplementary experiments are designed to examine the STBB system's multimodal decoupling capability in varying motion conditions. Firstly, different rotational speeds are applied while keeping the vibration frequency constant. Secondly, different vibration frequencies are applied under a fixed rotational speed. The results are shown in Fig. 4h and i, respectively. Fig. 4h presents the frequency spectra under different rotational speeds ranging from 100 to 1000 rpm. In each case, a single prominent spectral peak appears at the frequency corresponding to the actual rotational speed (e.g., 101.45 rpm, 301.29 rpm, 500.99 rpm). The peaks stand out significantly from the background noise, and the deviation in the calculated speed is within $\pm$1.45%. These results reflect the precision of the proposed DFT algorithm. They also benefit from the specially designed mosaic-patterned electret and its corresponding induction electrode, which ensure stable and controllable charge induction during rotation. This structure provides a high signal-to-noise ratio and a clean input for frequency-domain analysis, enabling accurate extraction of rotational features. Fig. 4i shows the frequency spectra obtained under various vibration frequencies (5–20 Hz) with a fixed rotational speed. After applying envelope extraction and a second FFT, each resulting spectrum shows a distinct spectral peak precisely at the frequency matching the imposed excitation (e.g., 5.01 Hz, 7.02 Hz, 12.03 Hz, 20.06 Hz). The deviation from the expected frequency remains within $\pm$2%. These results are attributed to the high sensitivity of the electrode structure to radial perturbations, which enhances the detectability of low-frequency modulation. When combined with the proposed decoupling algorithm, the system enables effective separation and accurate identification of low-frequency vibration features.

In conclusion, the proposed STBB achieves robust and high-precision decoupling of rotational and vibrational signals under various complex motion conditions by integrating a novel mosaic-patterned electret film and electrode with the DFT algorithm. This demonstrates its excellent potential for accurate and reliable multimodal sensing in practical applications.

2.5. Industrial application and fault diagnosis

In the field of industrial intelligent manufacturing, thrust ball bearings are critical components in motion systems, and their condition monitoring directly impacts the reliability and safety of equipment operation. The automotive assembly line serves as a representative application scenario, as shown in Fig. 5a. Based on this context, a practical bearing fault monitoring system is implemented for industrial applications. The workflow of the designed bearing fault monitoring system is illustrated in Fig. 5b. During normal operation, the electret film of the STBB maintains a stable surface charge, which induces a time-varying voltage on the adjacent electrodes through electrostatic interaction. The voltage is collected and preliminarily processed by the circuit module to ensure signal integrity and accuracy. The processed signals are transmitted wirelessly via a Bluetooth module to the host computer system. Upon reception, the host computer performs real-time calculation and analysis using its built-in signal processing module. Feature extraction and the DFT algorithm are applied to analyze the vibration signals in depth, identifying potential fault characteristics such as misalignment and abnormal vibrations. The analysis results are displayed in real time via a host computer, providing operators with intuitive information on bearing conditions. The circuit-integrated STBB system is deployed on a robotic arm test platform that simulates an automotive assembly line (Fig. S5), enabling in-situ signal acquisition, wireless transmission, and intelligent diagnosis. This system thus enables real-time monitoring and fault diagnosis of bearing operational status.

Furthermore, the STBB's application in bearing fault diagnosis is explored. Five representative fault types commonly observed in industrial environments are simulated: rotor damage, stator damage, displacement, overturning, and sudden speed variation. The corresponding output signals for these faults are shown in Fig. 5c. The waveform characteristics differ distinctly across fault scenarios, demonstrating the feasibility of fault type discrimination based on the STBB's outputs.

In practical applications, these faults are often imperceptible to the naked eye. Despite the superior sensing performance of the proposed STBB, which capture distinct data variations under faulty conditions, timely manual detection remains a significant challenge. Consequently, the integration of an automated detection and early-warning system is of paramount importance. Deep learning, characterized by its robust autonomous feature extraction and capacity to model complex nonlinear patterns, can substantially enhance recognition accuracy and reliability in intricate industrial environments. Specifically, the "gating mechanism" (comprising forget, input, and output gates) inherent in Long Short-Term Memory (LSTM) networks—as illustrated in Fig. S6a—enables the autonomous learning and retention of long-term temporal dependencies within data sequences.

In this study, a four-layer LSTM neural network was constructed, with detailed parameters provided in Table S3. To mitigate the risk of overfitting, dropout layers were incorporated to selectively discard redundant features with lower weights during processing. The network eventually outputs various fault categories shown in Fig. 5c via one-hot encoding. For dataset construction, 100 sets of signal profiles were collected for each scenario (including normal operation). Each signal lasts for 1 s and comprises 1000 data points, ensuring that the temporal characteristics of each fault are fully captured. To further enhance the model's robustness, five types of random noise (Gaussian, impulse, multiplicative, and temporal shift noise) were applied to the original data, expanding the dataset fivefold. The augmented dataset was partitioned into training, validation, and testing sets in a ratio of 60:20:20. During the training phase, early stopping and L2 regularization were implemented to prevent overfitting. The convergence of the model, characterized by the evolution of accuracy and loss functions for both training and testing sets, is presented in Fig. S6b.

Fig. 5d shows the t-distributed stochastic neighbor embedding (t-SNE) visualization of the fully connected layer outputs from the test sets, with data points colored according to real labels. Clusters corresponding to different fault types are well separated, confirming the model's capability to distinguish among fault categories.

An integrated monitoring system was developed based on the trained LSTM neural network to facilitate visualized automatic detection and real-time early warning, with its operational workflow detailed in Fig. 5e. Specifically, data acquired by the STBB under diverse and complex operating conditions undergo data augmentation and training within the LSTM framework to optimize and preserve model parameters. To ensure high temporal resolution and real-time performance, a sliding window mechanism is employed for seamless data transmission. While a dedicated background thread continuously processes and displays the raw STBB signals, the windowed data segments are concurrently fed into the neural network for inference and condition identification. Furthermore, an intuitive decision-support interface is implemented; it features a dynamic feedback mechanism that triggers specific fault-type visualizations according to the identified categories, thereby enabling comprehensive situational awareness of industrial operations.

Two typical bearing fault modes are selected for experimental validation. As shown in Fig. 5f, a notch is introduced into the electrode to simulate electrode damage in the STBB. Under this fault condition, the collected voltage signals exhibit alternating high and low peaks. Following signal analysis by the host computer, the real-time display interface, presents the corresponding voltage waveform and issues a bearing condition warning. Fig. 5g simulates the scenario of bearing eccentric misalignment during operation. In this case, the upper and lower components of the bearing experience relative rotation and displacement, resulting in unstable and chaotic voltage signal peaks. The real-time display interface promptly detects and displays the fault condition, issuing a corresponding warning. Experimental validation confirms that the proposed bearing monitoring system performs reliably and effectively under complex operating conditions. This robust performance provides strong technical support for predictive maintenance in industrial manufacturing environments. Fig. 5h presents the probability distribution matrix for the six scenarios. The high intensity along the diagonal elements demonstrates high classification accuracy across typical fault cases. Quantitatively, the overall diagnostic accuracy achieved by the LSTM classifier is 90.33%, highlighting the effectiveness and precision of the proposed STBB system in intelligent fault diagnosis.

3. Conclusion

In this study, we introduce a selective mosaic-patterned electret charging method together with a dedicated electrode layout. The resulting discretized charge distribution provides distinct signal modulation patterns under different motion modes, enabling the sensing module to effectively distinguish and characterize the rotational and vibrational components of bearing motion. In addition, the structural adaptability of this design offers practical extensibility and provides a viable reference for multi-modal monitoring across different types of bearings. Building on this sensing architecture, the STBB exhibits stable and reliable performance under single-mode conditions. The sensor achieves a rotational sensitivity of 7.48 rpm·Hz^{-1} with a correlation coefficient of $R^2 = 0.9999$, and maintains a highly linear frequency response in the 2–20 Hz vibration range with a correlation coefficient of $R^2 = 0.9998$. Under coupled motion, the dual Fourier transform-based decoupling strategy clearly separates the rotational and vibrational components, with relative errors controlled at 0.23% and 0.15%, respectively. The result demonstrates the feasibility and accuracy of the proposed approach for multi-modal motion recognition in practical bearing environments. The STBB was further applied to a six-joint robotic arm to conduct system-level functional validation. By simulating multiple representative industrial fault conditions and collecting the corresponding multi-modal response signals, an experimental dataset was constructed for training an LSTM-based diagnostic model. Leveraging the real-time data stream provided by the STBB, the classifier successfully distinguishes six operating states with an overall diagnostic accuracy of 90.33%. These results confirm that the proposed STBB platform combines high sensitivity, robustness, signal decoupling, and intelligent diagnostic capabilities, making it a potential candidate for scalable deployment in predictive maintenance systems. While the present study focuses on controlled experimental validation, future work will further investigate long-term operational stability in real industrial environments, extend the diagnostic framework to larger and more diverse fault datasets, and explore adaptive gap-compensation strategies for extreme operating conditions.

4. Experimental section

4.1. Fabrication of the STBB

The STBB proposed in this study consists of the electret film and electrodes, both featuring concentric annular geometries. The outer diameter is 60 mm, the inner diameter is 38.5 mm, and the axial width is 10.75 mm. The electret substrate and stator electrodes are fabricated using printed circuit board (PCB) technology on a 0.6 mm-thick FR-4 epoxy glass fiber laminate. The electrodes are arranged in 16 sector-shaped regions, each with a central angle of 43.5°, alternately connected as positive and negative poles. The inner and outer electrode rings are concentrically aligned, and a constant angular gap is maintained between adjacent sectors to ensure uniform electric field distribution during rotation. The bearing elements are made of GCr15 bearing steel, chosen for its excellent wear resistance and dimensional stability.

4.2. Assembly of the test platform

To evaluate the response of the STBB under different dynamic conditions, an experimental platform was constructed, integrating both rotational and vibrational excitation modules. A stepper motor from the 57 series (Model: 57HD7416-21B) was employed to provide adjustable-speed rotation of the bearing rotor. Simultaneously, a vibration exciter (Model: SA-JZ002) was used to apply radial disturbances, simulating compound motion states typically encountered in real-world applications. The STBB was rigidly mounted onto the platform via a base, while the shaft ring was coupled to the motor's output shaft to ensure stable and continuous rotation.

4.3. Signal acquisition and data processing

The electrostatic signals generated during STBB operation were collected using a high-precision electrometer (Keithley 6514, Tektronix). The sampling frequency was set to 1 kHz to accurately capture dynamic features at high resolution. The acquired raw signals were then analyzed using MATLAB for filtering, Fourier transform, frequency spectrum extraction, and phase feature analysis.

CRediT authorship contribution statement

Longwei Duan: Writing – original draft, Validation, Software, Methodology, Formal analysis, Data curation. **Xinhui Mao:** Validation, Investigation, Formal analysis. **Yuxiang Dong:** Software, Formal analysis. **Haiyang Yu:** Validation, Investigation, Formal analysis, Data curation. **Jiyuan Zhang:** Supervision, Formal analysis, Data curation. **Shuyu Zhang:** Software. **Yiqun Gu:** Writing – original draft, Supervision. **Yingwen Li:** Visualization. **Kaifeng Ding:** Data curation. **Zhiheng Wang:** Data curation. **Xingxu Zhang:** Conceptualization. **Honglong Chang:** Supervision, Conceptualization. **Lihua Tang:** Writing – review & editing, Supervision, Conceptualization. **Jin Wu:** Writing – review & editing, Methodology, Conceptualization. **Wenbin Huang:** Writing – review & editing, Supervision, Conceptualization. **Kai Tao:** Writing – review & editing, Supervision, Methodology, Conceptualization.

Declaration of competing interest

The authors declare that they have no known competing financial interests or personal relationships that could have appeared to influence the work reported in this paper.

Acknowledgements

This research is supported by National Natural Science Foundation of China (52575670), Shenzhen Science and Technology Program (JCYJ20220530161809020 & JCYJ20220818100415033), GuangDong Basic and Applied Basic Research Foundation (2024A1515012324), The Key Research and Development Program of Shaanxi Province (2024GX-YBXM-193). These authors contributed equally: Longwei Duan, Xinhui Mao, Yuxiang Dong.

Appendix A. Supplementary data

Supplementary data to this article can be found online at https://doi.org/10.1016/j.cej.2026.174378.

Data availability

Data will be made available on request.

References

[1] S. Gao, S. Zhang, Y. Zhang, Y. Gao, Operational reliability evaluation and prediction of rolling bearing based on isometric mapping and NoCuSa-LSSVM, Reliab. Eng. Syst. Saf. 201 (2020), https://doi.org/10.1016/j.ress.2020.106968.

[2] F.-J. Ebert, An overview of performance characteristics, experiences and trends of aerospace engine bearings technologies, Chin. J. Aeronaut. 20 (4) (2007) 378–384, https://doi.org/10.1016/s1000-9361(07)60058-2.

[3] E. Desnica, D. Mikić, H. Glavaš, I. Palinkaš, Influence of diagnostics on bearing reliability on robotic systems, Adv. Eng. Lett. 1 (2) (2022) 40–45, https://doi.org/10.46793/adeletters.2022.1.2.2.

[4] B. Xia, K. Wang, A. Xu, P. Zeng, N. Yang, B. Li, Intelligent fault diagnosis for bearings of industrial robot joints under varying working conditions based on deep adversarial domain adaptation, IEEE Trans. Instrum. Meas. 71 (2022) 1–13, https://doi.org/10.1109/tim.2022.3158996.

[5] Y. Guo, S. Sheng, C. Phillips, J. Keller, P. Veers, L. Williams, A methodology for reliability assessment and prognosis of bearing axial cracking in wind turbine gearboxes, Renew. Sustain. Energy Rev. 127 (2020), https://doi.org/10.1016/j.rser.2020.109888.

[6] Y. Liu, G. Ma, L. Zhu, H. Wang, C. Han, Z. Li, H. Wang, Q. Yong, Y. Huang, Structure–performance evolution mechanism of the wear failure process of coated spherical plain bearings, Eng. Fail. Anal. 135 (2022), https://doi.org/10.1016/j.engfailanal.2022.106097.

[7] Y. Liu, W. Zheng, B. Liu, X. Zhu, S. Jiang, S. Pei, Wear behavior analysis of graphite bearings in aircraft fuel pumps under mixed lubrication, Wear 584-585 (2026) 206390, https://doi.org/10.1016/j.wear.2025.206390.

[8] M. Wodtke, W. Litwin, G. van der Meer, R. van Ostayen, Wear tests of hydrodynamic journal bearings lubricated with magnetorheological fluid, Wear 584-585 (2026) 206404, https://doi.org/10.1016/j.wear.2025.206404.

[9] J. Lai, K. Stadler, Investigation on the mechanisms of white etching crack (WEC) formation in rolling contact fatigue and identification of a root cause for bearing premature failure, Wear 364-365 (2016) 244–256, https://doi.org/10.1016/j.wear.2016.08.001.

[10] S. Xiao, H. Li, Z. Zhan, G. Wu, Y. Cao, T. Li, X. Yan, J. Zeng, Q. Wang, Y. Pan, Y. Qian, G. Gao, Y. Guo, X. Zhang, Overvoltage-Induced bearing corrosion in High-Speed train traction motors: analysis and mitigation, Eng. Fail. Anal. 185 (2026) 110440, https://doi.org/10.1016/j.engfailanal.2025.110440.

[11] Z. Xia, Y. Wang, D. Wu, X. Zhang, Y. Li, L. Hao, J. Wang, E.-H. Han, Coupling mechanism of rolling contact fatigue and corrosion on bearing steel in brine contaminated lubricant oil under heavy load, Eng. Fail. Anal. 175 (2025) 109596, https://doi.org/10.1016/j.engfailanal.2025.109596.

[12] X. Shi, K. Kida, Y. Kashima, Surface crack and wear of PPS polymer thrust bearings under rolling contact fatigue in water, Mater. Res. Innov. 18 (sup5) (2014) S5-42–S5-47, https://doi.org/10.1179/1432891714z.000000000905.

[13] K. Kida, M. Saito, K. Kitamura, Flaking failure originating from a single surface crack in silicon nitride under rolling contact fatigue, Fatigue Fract. Eng. Mater. Struct. 28 (12) (2005) 1087–1097, https://doi.org/10.1111/j.1460-2695.2005.00947.x.

[14] F. Li, X. Li, H. Liu, S. Deng, Parameter investigation of bearing based on rolling–sliding contact fatigue crack growth considering load history, Mech. Mach. Theory 218 (2025) 106268, https://doi.org/10.1016/j.mechmachtheory.2025.106268.

[15] F. Xu, N. Ding, N. Li, L. Liu, N. Hou, N. Xu, W. Guo, L. Tian, H. Xu, C.-M. Lawrence Wu, X. Wu, X. Chen, A review of bearing failure modes, mechanisms and causes, Eng. Fail. Anal. 152 (2023), https://doi.org/10.1016/j.engfailanal.2023.107518.

[16] N. Tandon, G.S. Yadava, K.M. Ramakrishna, A comparison of some condition monitoring techniques for the detection of defect in induction motor ball bearings, Mech. Syst. Signal Process. 21 (1) (2007) 244–256, https://doi.org/10.1016/j.ymssp.2005.08.005.

[17] P. Lyu, K. Zhang, W. Yu, B. Wang, C. Liu, A novel RSG-based intelligent bearing fault diagnosis method for motors in high-noise industrial environment, Adv. Eng. Inform. 52 (2022), https://doi.org/10.1016/j.aei.2022.101564.

[18] D. Hou, H. Qi, D. Li, C. Wang, D. Han, H. Luo, C. Peng, High-speed train wheel set bearing fault diagnosis and prognostics: research on acoustic emission detection mechanism, Mech. Syst. Signal Process. 179 (2022), https://doi.org/10.1016/j.ymssp.2022.109325.

[19] G. Teng, C. Yang, A. Quan, C. Li, H. Li, Y. Cheng, H. Chang, M. Kraft, H. Zhang, Extracting mechanical quality factor and eliminating feedthrough using harmonics of thermal-piezoresistive micromechanical resonators, Microsyst. Nanoeng. 11 (1) (2025) 30, https://doi.org/10.1038/s41378-025-00869-8.

[20] L. Gong, Z. Zhang, R. Luan, Y. Feng, M. Gao, C. Zhang, Self-powered technologies for smart bearings, Fundam. Res. (2025), https://doi.org/10.1016/j.fmre.2025.04.007.

[21] K. Tao, J. Yu, J. Zhang, A. Bao, H. Hu, T. Ye, Q. Ding, Y. Wang, H. Lin, J. Wu, H. Chang, H. Zhang, W. Yuan, Deep-learning enabled active biomimetic multifunctional hydrogel electronic skin, ACS Nano 17 (16) (2023) 16160–16173, https://doi.org/10.1021/acsnano.3c05253.

[22] X. Mao, J. Zhang, L. Duan, B. Lyu, Y. Dong, F. Cao, C. Jia, L. Liu, H. Chang, Z. Li, K. Tao, AI-driven ocean monitoring with multimodal triboelectric nanogenerator: self-sustainable real-time wave warning and forecasting system, Nano Energy 140 (2025) 111004, https://doi.org/10.1016/j.nanoen.2025.111004.

[23] K. Tao, Z. Chen, J. Yu, H. Zeng, J. Wu, Z. Wu, Q. Jia, P. Li, Y. Fu, H. Chang, W. Yuan, Ultra-sensitive, deformable, and transparent triboelectric tactile sensor based on micro-pyramid patterned ionic hydrogel for interactive human–machine interfaces, Adv. Sci. 9 (10) (2022) 2104168, https://doi.org/10.1002/advs.202104168.

[24] Z. Wang, G. Liu, J. Cao, X. Fu, B. Fan, Y. Qin, Z. Wang, Z. Zhang, Y. Chen, C. Zhang, Self-powered position monitoring system based on insole-type wearable triboelectric nanogenerator and Bluetooth beacon, Adv. Mater. Technol. 8 (18) (2023), https://doi.org/10.1002/admt.202300487.

[25] K. Tao, H. Yi, Y. Yang, H. Chang, J. Wu, L. Tang, Z. Yang, N. Wang, L. Hu, Y. Fu, J. Miao, W. Yuan, Origami-inspired electret-based triboelectric generator for biomechanical and ocean wave energy harvesting, Nano Energy 67 (2020) 104197, https://doi.org/10.1016/j.nanoen.2019.104197.

[26] J. Li, Y. Zhang, X. Gao, Y. Mao, C. Hu, K. Long, C. Sun, S. Guo, Self-powered droplet sensor based on triboelectric nanogenerator toward the Internet-of-Things (IoT) alarm system, ACS Appl. Electron. Mater. 5 (11) (2023) 6026–6036, https://doi.org/10.1021/acsaelm.3c01018.

[27] L. Qin, L. Zhang, J. Feng, F. Zhang, Q. Han, Z. Qin, F. Chu, A hybrid triboelectric-piezoelectric smart squirrel cage with self-sensing and self-powering capabilities, Nano Energy 124 (2024), https://doi.org/10.1016/j.nanoen.2024.109506.

[28] X. Mao, J. Zhang, J. Zhang, Y. Gao, Y. Zhang, C. Zhang, P. Li, H. Wu, J. Wu, X. Zhang, T. Ye, K. Tao, DNA-helix-inspired Kirigami nanogenerator with dual-function energy absorption and conversion, Chem. Eng. J. 523 (2025) 168261, https://doi.org/10.1016/j.cej.2025.168261.

[29] H. Zhao, K. Fan, S. Zhao, S. Wu, X. Zhang, Z. Hou, Lightweight energy harvesting backpack achieved with a slingshot-inspired flexible accelerator, Appl. Energy 379 (2025), https://doi.org/10.1016/j.apenergy.2024.124993.

[30] L. Zhao, H. Zou, K. Wei, S. Zhou, G. Meng, W. Zhang, Mechanical intelligent energy harvesting: from methodology to applications, Adv. Energy Mater. 13 (29) (2023), https://doi.org/10.1002/aenm.202300557.

[31] Y. Zhang, J. Cao, H. Zhu, Y. Lei, Design, modeling and experimental verification of circular Halbach electromagnetic energy harvesting from bearing motion, Energ. Conver. Manage. 180 (2019) 811–821, https://doi.org/10.1016/j.enconman.2018.11.037.

[32] M.A. Halim, R. Rantz, Q. Zhang, L. Gu, K. Yang, S. Roundy, An electromagnetic rotational energy harvester using sprung eccentric rotor, driven by pseudo-walking motion, Appl. Energy 217 (2018) 66–74, https://doi.org/10.1016/j.apenergy.2018.02.093.

[33] X. Ma, H. Li, S. Zhou, Z. Yang, G. Litak, Characterizing nonlinear characteristics of asymmetric tristable energy harvesters, Mech. Syst. Signal Process. 168 (2022) 108612, https://doi.org/10.1016/j.ymssp.2021.108612.

[34] N. Sezer, M. Koç, A comprehensive review on the state-of-the-art of piezoelectric energy harvesting, Nano Energy 80 (2021) 105567, https://doi.org/10.1016/j.nanoen.2020.105567.

[35] X. Ma, H. Ma, S. Zhou, Nonlinear analysis and response identification of tristable energy harvesters under wind and base excitations, Int. J. Non-Linear Mech. 173 (2025) 105052, https://doi.org/10.1016/j.ijnonlinmec.2025.105052.

[36] Y. Dong, L. Duan, X. Mao, T. Gu, Y. Gu, H. Yu, X. Zhang, T. Ye, X. Wang, P. Li, J. Wu, H. Wu, K. Fan, L. Hu, F. Wang, L. Tang, K. Tao, Exploring human motions for smart wearables: energy conversion, harvesting and self–powered sensing, Nano Energy 143 (2025) 111289, https://doi.org/10.1016/j.nanoen.2025.111289.

[37] Y. Yang, J. Wen, F. Chen, Y. Hao, X. Gao, T. Jiang, B. Chen, Z.L. Wang, Barycenter self-adapting triboelectric nanogenerator for sea water wave high-entropy energy harvesting and self-powered forecasting in marine meteorology, Adv. Funct. Mater. 32 (24) (2022), https://doi.org/10.1002/adfm.202200521.

[38] Y. Cao, W. Shen, F. Li, H. Qi, J. Wang, J. Mao, Y. Yang, K. Tao, All-in-one high-power-density vibrational energy harvester with impact-induced frequency broadening mechanisms, Micromachines 12 (9) (2021), https://doi.org/10.3390/mi12091083.

[39] K. Tao, L. Tang, J. Wu, S.W. Lye, H. Chang, J. Miao, Investigation of multimodal electret-based MEMS energy harvester with impact-induced nonlinearity, J. Microelectromech. Syst. 27 (2) (2018) 276–288, https://doi.org/10.1109/jmems.2018.2792686.

[40] K. Tao, Z. Zhao, Y. Yang, J. Wu, Y. Li, K. Fan, Y. Fu, H. Chang, W. Yuan, Development of bipolar-charged electret rotatory power generator and application in self-powered intelligent thrust bearing, Nano Energy 90 (2021), https://doi.org/10.1016/j.nanoen.2021.106491.

[41] W. Wang, N. Yin, Z. Wu, Z. Zhang, Omnidirectional energy harvesting with 3D-TENG for vibration diagnosis, Chem. Eng. J. 509 (2025) 161022, https://doi.org/10.1016/j.cej.2025.161022.

[42] J. Yang, Y. Sun, J. Zhang, B. Chen, Z.L. Wang, 3D-printed bearing structural triboelectric nanogenerator for intelligent vehicle monitoring, Cell Rep. Phys. Sci. 2 (12) (2021), https://doi.org/10.1016/j.xcrp.2021.100666.

[43] P. Ji, J. Wen, X. Gao, H. Li, H. Cai, K. Lv, Z.L. Wang, B. Chen, Roadbed tribological energy harvester, Sci. Adv. 11 (25) (2025) eadv9379, https://doi.org/10.1126/sciadv.adv9379.

[44] F. Xing, X. Gao, W. Gao, Y. Sun, Z. Zhao, Z.L. Wang, B. Chen, High-entropy energy for self-powered systems, SmartSys 1 (2) (2025) e70001, https://doi.org/10.1002/sys3.70001.

[45] Q. Han, Z. Ding, Z. Qin, T. Wang, X. Xu, F. Chu, A triboelectric rolling ball bearing with self-powering and self-sensing capabilities, Nano Energy 67 (2020), https://doi.org/10.1016/j.nanoen.2019.104277.

[46] D. Choi, T. Sung, J.Y. Kwon, A self-powered smart roller-bearing based on a triboelectric nanogenerator for measurement of rotation movement, Adv. Mater. Technol. 3 (12) (2018), https://doi.org/10.1002/admt.201800219.
[47] Y. Zhang, H. Zhu, Y. Xu, J. Cao, S. Bader, B. Oelmann, Theoretical modeling and experimental verification of rotational variable reluctance energy harvesters, Energy Convers. Manag. 233 (2021), https://doi.org/10.1016/j.enconman.2021.113906.
[48] Z. Wang, W. Wang, F. Gu, C. Wang, Q. Zhang, G. Feng, A.D. Ball, On-rotor electromagnetic energy harvester for powering a wireless condition monitoring system on bogie frames, Energy Convers. Manag. 243 (2021), https://doi.org/10.1016/j.enconman.2021.114413.
[49] L. Zhang, F. Zhang, Z. Qin, Q. Han, T. Wang, F. Chu, Piezoelectric energy harvester for rolling bearings with capability of self-powered condition monitoring, Energy 238 (2022), https://doi.org/10.1016/j.energy.2021.121770.
[50] M. Guan, W.-H. Liao, Design and analysis of a piezoelectric energy harvester for rotational motion system, Energ. Conver. Manage. 111 (2016) 239–244, https://doi.org/10.1016/j.enconman.2015.12.061.
[51] Z. Li, X. Wang, T. Fu, Y. Hu, L. Li, Z. Zhao, L. Wu, C. Wang, S. Zhang, Research on nano-film composite lubricated triboelectric speed sensor for bearing skidding monitoring, Nano Energy 113 (2023), https://doi.org/10.1016/j.nanoen.2023.108591.
[52] R. Abraham, P. Simon, Review on mosaicing techniques in image processing, in: 2013 Third International Conference on Advanced Computing and Communication Technologies (ACCT), 2013, pp. 63–68.